






Lensless, reflection-based dark-field microscopy (RDFM) on a CMOS chip

MERUYERT IMANBEKOVA,^{1,2}  AYYAPPASAMY SUDALAIYADUM PERUMAL,^{1,2} SARA KHEIREDDINE,¹  DAN V. NICOLAU,¹ AND SEBASTIAN WACHSMANN-HOGIU^{1,*} 

¹Department of Bioengineering, McGill University, Montreal, Quebec, H3A 0E9, Canada

²Equal contributions

*sebastian.wachsmannhogiu@mcgill.ca

Abstract: We present for the first time a lens-free, oblique illumination imaging platform for on-sensor dark-field microscopy and shadow-based 3D object measurements. It consists of an LED point source that illuminates a 5-megapixel, 1.4 μm pixel size, back-illuminated CMOS sensor at angles between 0° and 90° . Analytes (polystyrene beads, microorganisms, and cells) were placed and imaged directly onto the sensor. The spatial resolution of this imaging system is limited by the pixel size ($\sim 1.4 \mu\text{m}$) over the whole area of the sensor ($3.6 \times 2.73 \text{ mm}$). We demonstrated two imaging modalities: (i) shadow imaging for estimation of 3D object dimensions (on polystyrene beads and microorganisms) when the illumination angle is between 0° and 85° , and (ii) dark-field imaging, at $>85^\circ$ illumination angles. In dark-field mode, a 3–4 times drop in background intensity and contrast reversal similar to traditional dark-field imaging was observed, due to larger reflection intensities at those angles. With this modality, we were able to detect and analyze morphological features of bacteria and single-celled algae clusters.

© 2020 Optical Society of America under the terms of the [OSA Open Access Publishing Agreement](#)

1. Introduction

Light microscopy is one of the oldest scientific techniques and a key instrument in modern research. Lens-based microscopes are the most broadly used light microscopy systems. Yet, the ability to perform high spatial resolution imaging at enhanced magnification leads to limited field-of-view (FOV) and optical aberrations that distort the resulting image. To overcome the limitations of lens-based approaches, image stitching can be implemented to form mosaics with a large overall FOV of high-resolution images. However, such techniques require long acquisition times and can result in artifacts that are especially apparent at the overlap regions between the individual tiles [1]. Mobile phones can serve as a practical, portable imaging platform, where a suitable compromise between spatial resolution and FOV can be found based on the camera specifications. There are many reports describing mobile phones as biomedical imaging devices that can be used for health-related imaging [2–4] and environmental applications [5,6].

Lens-free approaches that typically use CMOS cameras found in mobile phones further simplify the hardware of imaging systems, whereby the sample is placed between the image sensor and the illumination source. One example is in-line holography, where the sensor detects shadows and diffraction interference patterns generated by the object, and the final image is reconstructed using computational algorithms. Whereas the FOV is limited by the sensor area, the spatial resolution can reach sub-pixel proportions using ptychographic imaging, where multiple images of the sample are taken at different illumination angles followed by image reconstruction [7,8]. Such approaches can also be used for imaging biological samples [9–15], nanoparticles [16,17] and can serve as portable and adaptable devices with minimal hardware requirements. However, these advantages come at a cost, which in this case is the computationally heavy holographic reconstruction, that eventually makes the system more complex.

Lens-free shadow imaging technologies have been successfully applied to various in vitro cellular applications [18–22]. However, the determination of micrometer-scale object size by existing systems without performing computing-intensive image reconstruction is an ongoing challenge. Cell size and volume are crucial parameters that have a significant impact on cell proliferation [23], response to environmental triggers [24], cellular homeostasis [25], and synaptic transmission [26]. Traditional techniques for micrometer-scale object size measurements such as flow cytometry and coulter counter are able to accurately detect the cell size in the range of tens of micrometers. However, the high cost of these methods limits their application to point-of-need applications. In addition to biological objects, the size of the particles within powders [27], emulsions [28], and aerosols [29] can influence the properties of these materials.

Non-holographic on-chip imaging, on the other hand, combines the conventional hardware design of lens-free imaging with ease of image acquisition, since complicated image reconstruction is not required in this case [30]. In terms of biological applications, direct on-chip sensing has been used to characterize individual cell types on microscope slides [31], and within microfluidic devices [32], study the behavior of *C. elegans* [33], detect cells that exhibit chemiluminescence [34] and has been adapted for sub-pixel resolution imaging [35,36].

While lens-based, and to some degree lens-free holographic technologies, can be implemented in numerous different or combined modalities, direct on-chip lens-free microscopy is still limited to transmission-based imaging. One of the potential new modality that will expand the existing range is dark-field microscopy.

Dark-field microscopy is an elegant optical technique, that allows extremely sensitive imaging due to its very low background and enhanced contrast of unstained objects. From the time of Van Leeuwenhoek, microscopists noted that some objects were more readily seen by applying oblique illumination that caused the darkening of the background while the object was visible due to the scattering of the oblique light. Since then, dark-field microscopy has been widely applied to image unstained biological samples [37–39] and nanoparticles [40,41]. In the last decade, several groups of researchers reported dark-field microscopy using a CMOS sensor for imaging mainly metal nanoparticles. Z. Li et al., reported a miniaturized dark-field microscope based on a CMOS sensor and microfluidic chip [42]. Further work by Grishin et al. showed a 3D-nanoparticle and microparticle tracking technique based on dark-field microscopy [43]. Previously we reported a dual-phone illumination-imaging microscope that is able to perform various modalities of traditional microscopes, including dark-field [44] and phase contrast [45]. However, while these systems are potentially simpler and less expensive than dark-field microscopes, they still use lenses to achieve oblique illumination or for imaging.

Here we present for the first time a reflection-based lens-free directly on the sensor imaging system with oblique illumination for dark-field imaging and object height measurement of non-biological and biological objects of micrometer size. We show that by measuring the shadow length of the object, we can calculate the approximate height of the objects such as polystyrene microspheres and bacteria. Moreover, by illuminating the sensor surface at large angles, we observed a significant reduction of the background intensity and reversal of the contrast for the objects of interest. This is due to higher reflection intensities at those large angles (in accordance with Fresnel equations of reflection) and is the equivalent of the dark-field illumination mode normally seen in lens-based microscopes.

In our platform, the light beam from an incoherent illumination source is situated at a distance much larger than the size of the CMOS sensor or the LED such that it can be considered a point source. This beam is partially reflected, refracted, or scattered at the interface between the two different optical media. When the sample of interest placed on the CMOS sensor is illuminated from the top (0° angle), most of the light is transmitted and reaches the photosensitive area of the photodiode. As a result, the resulting image has a typical bright field appearance. On the other hand, when the angle of the incident light is close to 90° , most of the light is reflected and only a

small amount of light is refracted, which, together with the scattered light from the sample, reach the photosensitive area of the detector. Subsequently, the background intensity of the images drops significantly, which leads to a better contrast of the object.

2. Experimental methods

2.1. Chemicals

Phosphate buffer saline (PBS) and ethanol were purchased from Sigma-Aldrich (USA). Sulfate latex particles (8% w/v) of 1.6 μm diameter were purchased from Invitrogen (USA). Polystyrene microspheres (50 mg/ml) of 7 μm diameter were purchased from Microspheres-Nanospheres (USA).

2.2. Lensless imaging platform

The imaging sensor is a back-illuminated 5-megapixel (MP) sensor module (OV5647, OmniVision technologies) with a 2592×1944 active array, and 8-/10-/24-bit RGB/RAW image output. The original lens and IR filter were removed in this set-up to achieve lensless imaging, and the sensor surface was thoroughly characterized via SEM and AFM (Fig. 1). Next, we applied a thin layer of a polymer (polydimethylsiloxane) onto the edges of the sensor in order to protect the electrical circuitry surrounding the immediate sensor area.

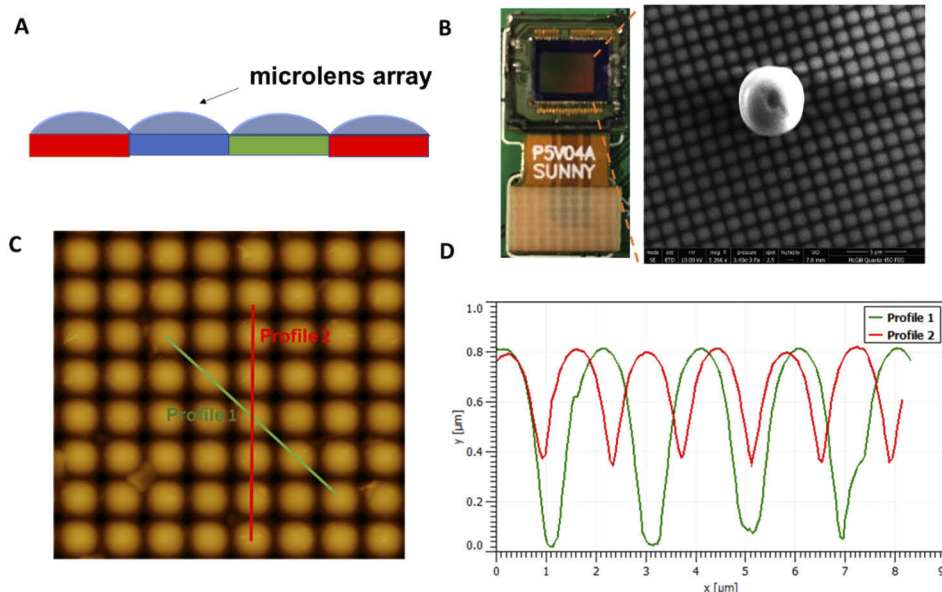


Fig. 1. CMOS sensor surface characterization. (A) Schematic illustration of the image sensor surface. (B) Photographic image of the CMOS sensor (left) and Scanning Electron Microscopy (SEM) image of a 7 μm bead on the sensor surface (right). (C) AFM image of the CMOS sensor surface. (D) AFM profile of the sensor surface and measurement of the height of the microlenses array.

Image acquisition and image processing were performed by via Raspberry Pi 3 Model B board using the Python programming language. Note that the FOV of the image sensor is the same as the active area and is 3.67×2.73 mm. The spatial resolution of the system is limited by the pixel size and is 1.4 μm .

We designed a multi-angle illumination platform that consists of three rulers set perpendicular to each other in XYZ directions. The X axis ruler provides the horizontal support and has

a digital angle finder that allows precise measurement of the incident angle (Fig. 2). The Y axis ruler provides adjustment for the height of the light source to achieve certain angles of illumination. As a source of incoherent light, we used a single cool white light LED with the wavelength range approximately 420-700 nm, diameter less than 1 mm and a remote controller for intensity modulation (SUSAY Electronics technology, China, model number NI-TL). The LED is mounted onto the Z axis holder that travels in a semi-circular path above the CMOS sensor, thereby creating a radius of 270 mm from the center of the sensor to the light source. Since the distance between the LED and the CMOS sensor is much larger than their physical dimensions, the illumination can be considered as a point source. The CMOS sensor was placed on a Z-adjustable stage and illuminated from various angles from 90° (oblique angle) up to 0° (top illumination). A droplet of polystyrene beads (5 μ L) of different sizes 1.6 μ m and 7 μ m was added directly onto the sensor surface and allowed to dry. We then imaged the beads under multiple angles, ranging from 0° (top) angle to 90° (oblique) angle.

To capture the image, we used a custom Python code to acquire standard JPEG images and raw Bayer data. The raw Bayer data is the data from the camera sensor prior to GPU processing such as demosaicing, auto white balance, smoothing etc. This data output is important in this work in order to be able to quantify the change in the image background. The raw Bayer image has a green and dark output appearance due to the BGGR pattern that has twice as many green pixels as red and blue. The raw images were saved to the camera as 6 MB data files, followed by extracting the PNG images that allow lossless compression of files. Afterwards, images were further analysed by additional software packages as described in the following section.

After imaging, the sensor can be effectively cleaned by pipetting a few microliters of 70% ethanol onto the sensor surface and gently wiping with lens tissue. The sensor can then be reused without any noticeable alterations in image quality.

2.3. *Bead-size quantification based on shadow images*

ImageJ (NIH), GraphPad Prism 6, and MATLAB (MathWorks) were utilized to process and analyse all captured bead shadow images. In Fig. 2(C), the height of the objects H was calculated from geometrical considerations from the measurement of the length of the shadow cast by the object at an angle α . The length of the shadow was measured by using averaged gray scale intensity values of the indicated area measured from the image. The angle α is equal to $(90^\circ - \theta)$, where θ is the incidence angle (Fig. 2(A)). The height of the object is determined from the tangent of the angle α , for known shadow length and incidence angle.

2.4. *Characterization via scanning electron microscopy*

The structural properties of the surface of the sensor were characterized by SEM microscopy. All SEM images were obtained using FEI NanoSEM instrument with accelerating voltage of 10 kV under high vacuum mode.

2.5. *Characterization via atomic force microscopy*

The sensor surface was analyzed by AFM (Multi Mode 8, Bruker) contact mode using triangular cantilevers (Hi-Res-C, MicroMasch, Estonia) with a radius of curvature of 1 nm. The obtained images were analyzed by Gwydion software.

2.6. *Preparation of microorganisms*

Euglena gracilis and *Staphylococcus epidermidis* were purchased from Carolina Biological supply Company (USA). The chosen biological sample, *E. gracilis*, has pigmented organelles, chloroplasts, and hence a strong ability to scatter light effectively, which makes it an ideal sample for testing the dark-field illumination mode. *E. gracilis* cells range from 8-20 μ m in length, are oval in shape cells and are much larger than the previously tested 7 μ m beads. On the other

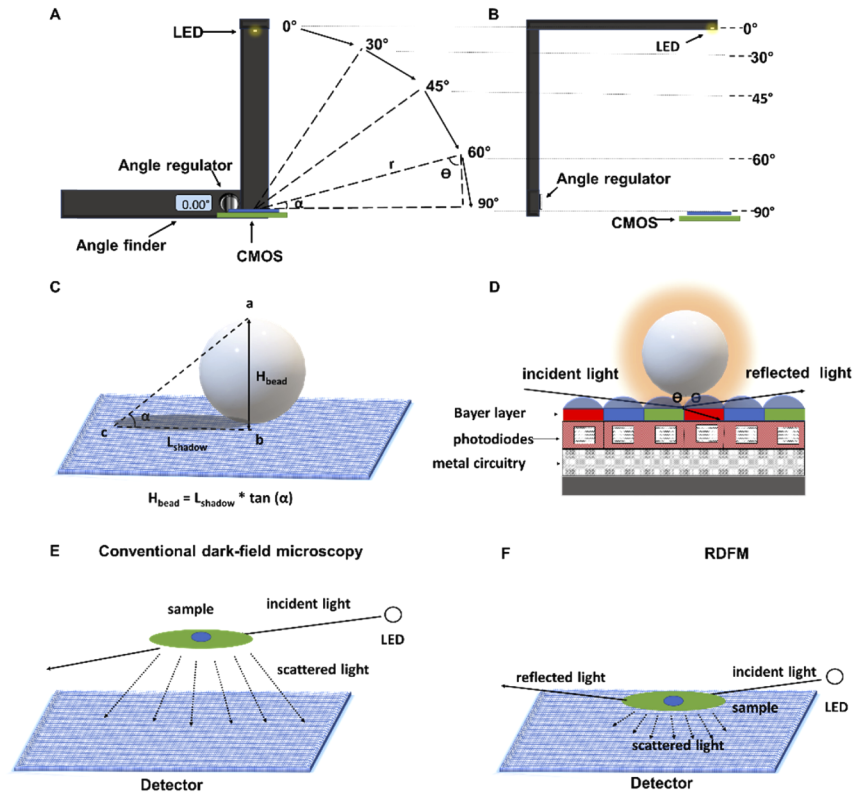


Fig. 2. Schematic of on-sensor dark-field microscopy via oblique angle illumination.

(A) Diagram of the illumination set-up (front view) that allows for multi-angle illumination ranging from 0° to 90° by rotating the point-like illumination source along a semicircle with radius r with the CMOS sensor placed in the center of the circle. (B) The side view diagram of the illumination set-up (C) Representation of a bead on the CMOS sensor. The shadow cast by the point source illumination is measured experimentally and the height of the object can be calculated based on a length of the shadow and known angle of incidence. (D) Schematic representation of the CMOS sensor and light illumination at a large angle. Microlenses are at the top layer, with the Bayer layer, photodiodes, and metal circuitry underneath. Microlenses focus the light onto the photodiodes such that a high fill factor can be achieved. The light beam travelling at a large angle reaches the sensor surface and gets reflected with the intensity of the reflected light obeying the Fresnel equations. The pixel fill factor also changes (is reduced) at shallow illuminations angles. These two phenomena lead to a change in the contrast and background intensities. (E) In conventional oblique illumination dark-field microscopy the sample of interest is placed at a distance from the sensor surface and illuminated at an oblique angle. The incident light rays will illuminate the sample, and the photons that are not scattered are either blocked or propagate next to the detector without being detected. Only scattered photons will be collected by the detector. (F) In RDFM, dark-field microscopy is achieved through Fresnel reflection of the incident light at the interface between air and the CMOS surface.

hand, *S. epidermidis* is a spherical bacterium with the body size ranging from 0.5-1.5 μm , whose dimensions are close to the resolving power of the pixels of this CMOS sensor. We grow *E. gracilis* at room temperature in a liquid Provasoli's enriched seawater (PES) medium that was prepared following the protocol in Handbook of Culture Media for Food and Water Microbiology [46]. The liquid PES culture was added directly onto the sensor surface, dried, and imaged. *S. epidermidis* colonies were cultured in a Nutrient broth (NB) medium at 30° overnight. Prior to incubation, a single colony of *S. epidermidis* was inoculated in 6 ml of NB medium. During the experiment, the liquid culture was added by pipetting directly onto the sensor surface or diluted beforehand if necessary.

3. Results and discussions

3.1. 3D geometrical measurements from shadow imaging

In order to demonstrate 3D geometrical measurements a droplet of microspheres of 7 μm and 1.6 μm in size was pipetted onto the sensor surface, dried and imaged at four angles of illumination. Figure 3(A) shows the shadow images of the 7 μm and 1.6 μm beads acquired at four different illumination angles. When the particle is illuminated by a source located above the sensor (0°), a shadow is cast right below the microsphere. The resulting images are used to evaluate the lateral dimensions of the object. Changing the angle of illumination will affect the projection of the shadow and increase the shadow length for larger angles, which in turn can be used for determination of the height of the object. Whereas shadow-based height estimation can be theoretically performed using multiple illumination angles, the choice of angle is important to be able to accurately delineate object-shadow boundaries. At small illumination angles (close to bright-field mode) as seen in Fig. 3(A) it is difficult to accurately determine the object-shadow boundaries especially in the cases where the size of the object is similar to the pixel size of the sensor. In addition, at small angles the shadow cast by the object lies beneath the object itself. Conversely, at large illumination angles, the object casts large shadows that can be measured as intensity drop. This makes the object-shadow boundaries discernable and measurable (Fig. 3(A)). Therefore, for the measurement of the height of micrometer-sized samples, the ideal illumination angle that provides the aforementioned conditions was found to be 84°. Next, using the images of the beads at 84° angle, we first obtained the plots of the grayscale intensity values across the background-bead-shadow-background region (blue rectangle), as shown in Fig. 3(B). The highest point in the plot (global maximum) represents the maximum scattering intensity generated by the bead. We then measured the cast shadow length starting from the global maximum marked in the graph, since part of the bead cast shadow lies under the object itself. Note, that this criterion of the shadow beginning is applicable for objects that are measured at 84° angle, as for lower angles the shadow lengths provide poor size estimates. The end of the cast shadow is identified by the point where the grayscale intensity values reach those of the background (plateau region). Since the best shadow measurements are obtained at large angles, one may think that further increasing the angle will provide better results. However, this is not the case, as at the larger illumination angles (87°-90°) we transition into a different regime, where scattering of the particles becomes predominant. This mode, which we call dark field mode, will be described in the following section (section 3.2). The distance between the photosensitive area of the pixels and the sample is relatively small and was not considered in the measurements of the shadow. However, the subtraction of the microlens array height (~800 nm) could possibly reduce the potential error in the object height measurements. Yet, the subtraction of the full microlens array height depends on the particles size and their distribution on the sensor surface, meaning that some particles will rest on top of the highest points of the microlens array, while others will fall into the gaps between adjacent microlenses (Fig. 1(D)). In the first scenario, the subtraction of the full size of the microlens array is more meaningful. On the other hand, the particles that are smaller than the gap between top ends of the adjacent microlenses (~1.93 μm along Profile 1, and ~1.4 μm along

Profile 2, Fig. 1(D)) will more likely lie at shorter distances from the sensor surface, which would warrant the subtraction of a reduced microlens height. Given this uncertainty, we calculated the size of the particles without any subtraction of the microlens array height. Knowing the size of the pixels, we were then able to calculate the shadow length in μm . Next, the height of microparticles of various sizes was measured by using the right triangle that is formed as depicted in Fig. 2(C), where H is the height of the microparticle, L is the shadow length, and α is the angle ($90^\circ - \theta$), where θ is the illumination angle. The estimated values of the height of the microparticles are presented in Table 1.

Table 1. Shadow-based object height estimation

Polystyrene bead size (μm)	The length of the shadow cast (pixels and μm)			The length of the shadow cast at 84° (pixels and μm)	Estimated height at 84° (μm)
	(0°)	(60°)	(80°)		
7 μm	5 pixels/7 μm	7 pixels/9.8 μm	29 pixels/40.6 μm	51.25 pixels/ 71.75 μm	~ 7.4 μm
1.6 μm	1-2 pixels/ 1.4-2.8 μm	4.5 pixels/ 6.3 μm	10.75 pixels/ 15.05 μm	10 pixels/ 14 μm	~ 1.5 μm

The results show a good correlation between the estimated height and the original size of the microspheres. Yet it is important to note that the microspheres were dispersed over the whole area of the CMOS sensor in order to achieve accurate height estimation. Estimation of the height of a denser sample will be more challenging as sample entities may have shadow regions nested within one another. For the reported range of angles, even with improved shadow contrast, the minimal distance between adjacent objects has to be large enough to completely cover the full length of the cast shadow, excluding the penumbra for simplicity. Recently, several groups have presented CMOS-based lens-free platforms for particle size and height measurements [20,21]. With respect to these measurements, the main difference between our platform and existing systems is the inherent simplicity. For example, while other methods for height measurements (such as those based on in line holography) require advanced computation techniques, in our platform the sample is placed onto the sensor surface and the shadow is directly measured from the resulting image. Moreover, the accuracy of the height estimate could be further improved by placing the sample even closer to the sensor surface by removing the microlenses and/or by using a CMOS chip with a smaller pixel size.

3.2. Dark-field microscopy on the CMOS sensor

In traditional microscopes, dark-field imaging is typically achieved by oblique illumination where the direct light is blocked from passing through the objective. The sample is placed at a certain distance from the sensor and the microscope objective collects only light that is scattered from the sample with minimal background or unscattered light, thus enhancing the contrast between the sample and the relatively dark background (Fig. 2(E)).

On the other hand, in a lens-free platform, the light beam reaches the sensor surface and the sensor collects both scattered and unscattered light from the sample. At large angles of incidence, according to the Fresnel equations of reflection, almost all the light is reflected leaving a small number of photons to be transmitted which leads to the darkening of the background. However, scattered light is mostly isotropic, and it will be collected by the detector. This leads to a microscopy mode where the scattering objects appear brighter than the background, similar to the dark-field microscopy mode (Fig. 2(F)).

In order to achieve dark-field illumination mode, we designed a configuration where the light is incident at large angles (close to 90° vs. the normal incidence to the surface of the sensor). This will make dark-field imaging possible even when blocking of the incident light is not possible such as for samples that are very close to the detector. The intensity of the reflected light at the

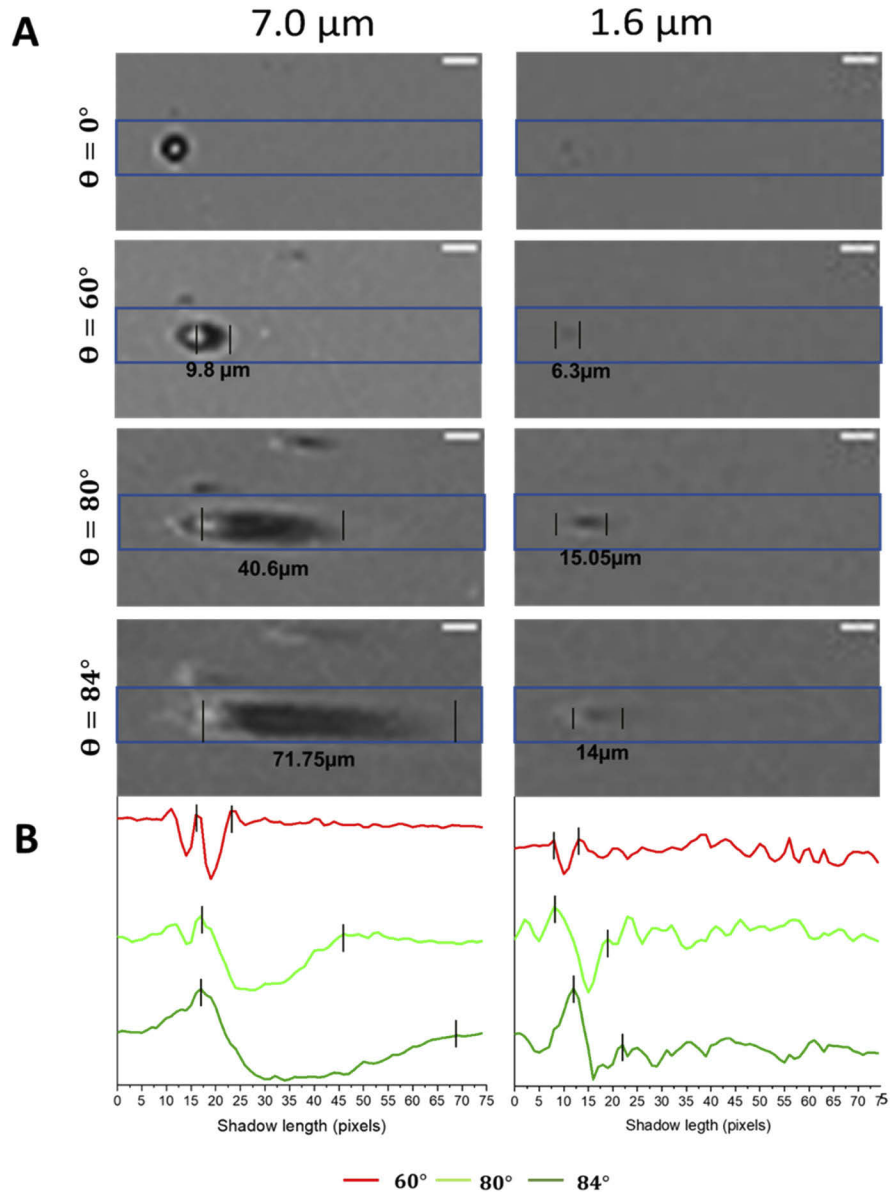


Fig. 3. Shadow measurements for estimation of object dimensions. (A) The length of the shadow increases as the illumination angle is increased from 0° to 84° for both 7 μm and 1.6 μm beads. (B) Plot of gray scale intensities measured within the blue rectangle. The length of the shadow changes can be measured for various angles of illumination and bead size. The scale bar in the inset corresponds to 10 μm .

interface between air (refractive index of 1) and the surface of the sensor (plastic, with a refractive index approximately 1.5) obeys the Fresnel equations such that at large angles of incidence, almost total reflection at this interface is expected. We explored this phenomenon as a modality of reducing the background in our images and recording scattered light similar to dark-field microscopy. In order to characterize the performance of this technique, we scanned across a sequence of incident angles starting from 84° up to 90° . For this, a droplet of microspheres of $7\ \mu\text{m}$ and $1.6\ \mu\text{m}$ in size was pipetted onto the sensor surface, dried and imaged at various angles of illumination. The blue lines on the image correspond to the ones depicted in the graph and aim to highlight the analyzed objects. As shown in Fig. 4, we observed a gradual change in background intensity starting from 84° of incidence angle and reaching a maximum darkening at 90° in processed as well as in raw images. We were still able to observe long shadows of the $7\ \mu\text{m}$ microspheres at angles between 84° up until 89° (Fig. 4(A)). On the other hand, at the 90° angle, the shadows disappeared and only scattering of the object was observed. The analysis of $1.6\ \mu\text{m}$ (Fig. 4(B)) showed similar trend in background intensity drop, yet the scattering intensity of the microspheres differed and was reduced due to the smaller size of the object. The raw images of the beads at top illumination angle show different patterns of coloration that could be explained by coloration artifacts generated at the level of RGB image processing. However, the observed coloration of the images does not affect in any way the analysis performed in this report. The graphs in Fig. 4(C) and 4(D) represent gray scale intensities of the raw and processed images of $7\ \mu\text{m}$ and $1.6\ \mu\text{m}$ microspheres. In order to calculate the decrease in background intensity, we also acquired an image without any incident light to be used as a baseline intensity (shown as a black dotted line in Fig. 4(C) and 4(D)). The graphs reveal a three to four times drop of the background intensity in the dark-field mode of the system in comparison with top illumination at 0° . This is at least three times lower than the expected drop that can be calculated from Fresnel equations, mainly due to the low flatness of the CMOS sensor (see Fig. 1) that leads to additional scattering. The calculated contrast values for the dark-field (90°) images of $7\ \mu\text{m}$ and $1.6\ \mu\text{m}$ beads are 0.3 for both, compared to 0.07 and 0.04, respectively, for the bright-field (0°) images.

Furthermore, the dark-field imaging set-up described here has been used for the detection of two or more clustered objects that are close to each other (Fig. 5).

When several objects are close to each other, the scattering intensity is proportional to the number of objects. According to the Mie scattering theory, the intensity of light scattered by micrometer-sized objects also depends on the object size angle of incidence, and wavelength of light. While we cannot distinguish between these phenomena, we observed and were able to detect clustered polystyrene beads of various sizes ($7\ \mu\text{m}$ and $1.6\ \mu\text{m}$) based on gray scale intensities (Fig. 5). A similar effect of detection using intensity differences has been further demonstrated using biological samples in the following sections.

3.3. Imaging of biological samples on the CMOS sensor

3.3.1. Reflection-based dark-field microscopy of biological objects and geometrical shadow-based height measurements

A $5\ \mu\text{l}$ droplet of *E. gracilis* liquid culture was pipetted onto the sensor surface that was previously hydrophilized with poly-L-lysine, followed by heat fixing. Two types of imaging were performed with *E. gracilis*, namely the shadow-based object height measurements as well as RFDM at large angles of illumination, i.e., $> 84^\circ$. Figure 6(A) represents the single *E. gracilis* cell at various angles of illumination. Here, we were able to observe the same gradual background drop as in previous experiments with polystyrene microspheres. Single *E. gracilis* cells were observed as bright shining objects on a dark background at illumination angles close to 90° . In Fig. 6(B), the depicted graph shows a gradual drop in the background intensity starting from 0° to an angle close to 90° , in agreement with Fresnel equations of reflection. The contrast values changed from 0.2 in the bright-field images to 0.6 in the dark field images. Next, we measured the height

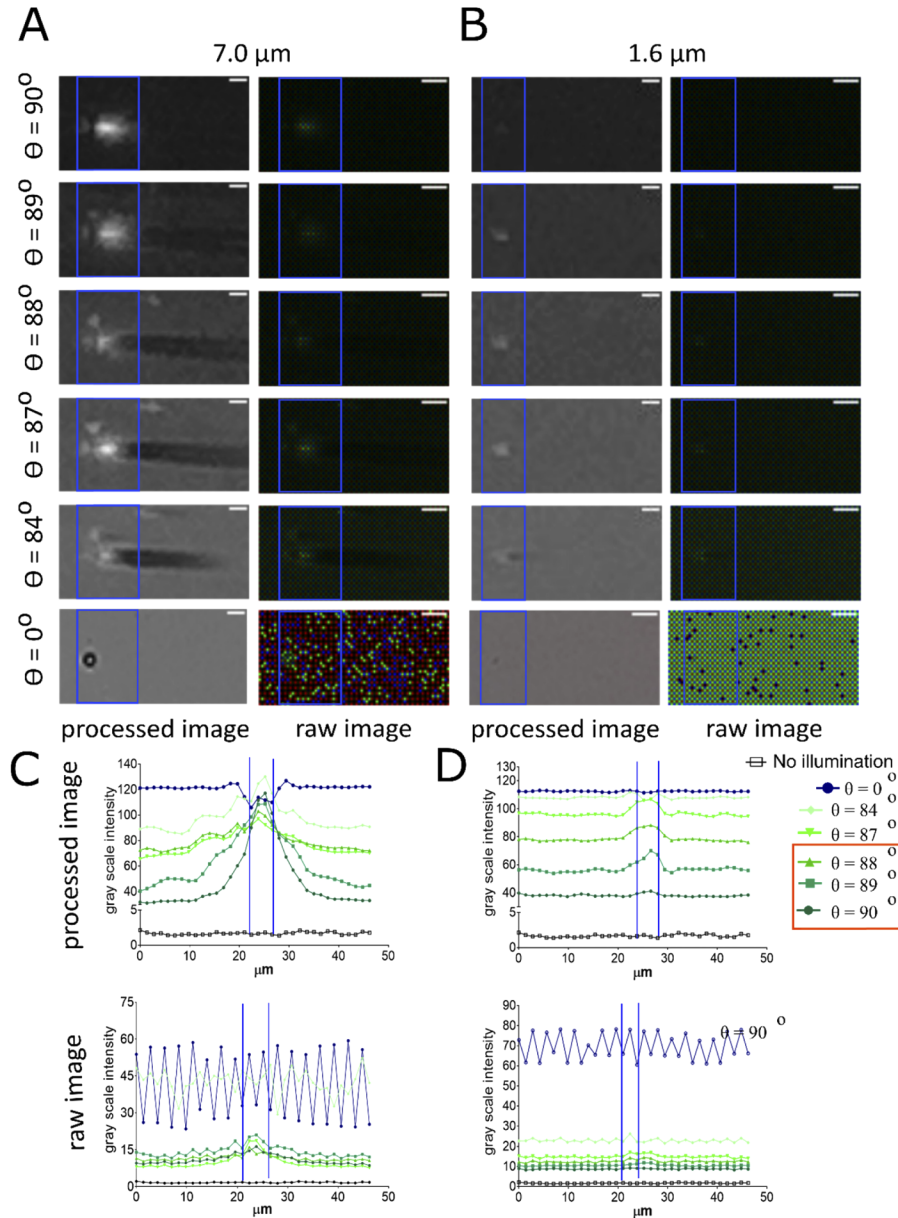


Fig. 4. Dark-field illumination mode. As the angle of incidence approaches 90° a gradual change in image contrast due to the decrease in background intensity for 7 μm (A) and 1.6 μm (B) beads can be observed. Panels A and B contain two sub-columns with processed images (left) and raw images (right) acquired from the Raspberry Pi. (C) and (D) represent two rows of graphs corresponding to processed (top) and raw (image) gray scale intensities. The background intensity drops three to four times at large angles. The drastic drop in background was more prominent in a narrow angle range, i.e., for illumination angles between 87° - 90° . (red box). The black dotted line corresponds to baseline intensities from a control image acquired in a completely dark room. The blue lines running vertically represent the borders for the areas used for plotting the graphs here and throughout this work. The scale bar corresponds to 10 μm .

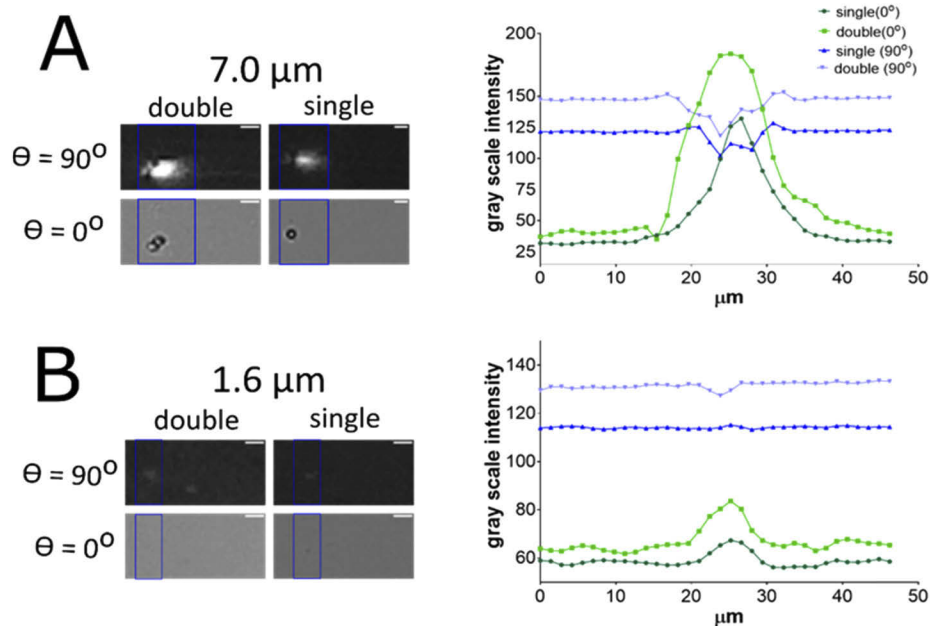


Fig. 5. Detection of clustered beads using the intensity of the reflected light at Fresnel reflection angles. Intensity difference for a single particle and two particles in close proximity for 7 μm sized (A) and also 1.6 μm sized beads (B). The graph at the right for the corresponding bead size illuminated at two different incident angles ($\theta = 90^\circ$ and $\theta = 0^\circ$) shows the variation of scattered light intensity depending on the number of clustered particles. The blue lines represent the borders used for plotting the graphs.

of *E. gracilis* based on a cast shadow length and the angle of incidence. Figure 6(C) depicts elongation of the *E. gracilis* shadows with a decrease of an incident angle. This effectively verifies the experimental results performed with polystyrene beads, showing the versatility of this system for fixed biological samples. Afterward, using the gray scale intensity plots, we measured the lengths of the cast shadows. The limits of the shadow were determined with the same method used for microspheres described above. The calculation of the height of the *E. gracilis* cells using determined shadow length and known incidence angle resulted to be $\sim 5 \mu\text{m}$. The result is consistent with *E. gracilis* dimensions previously reported in the literature, while taking into consideration the potential size reduction of the sample as a result of fixation. [47]. The measurement of the single *E. gracilis* length at a top angle is found to be between 10–11 μm for Fig. 6(A) and close to 15 μm for Fig. 6(C).

Following experiments with *E. gracilis*, *S. epidermidis* was used as a biological sample to demonstrate close-to-pixel resolution/visualization. A 5 μL droplet of the bacterial culture was mixed with 3% glutaraldehyde solution (1:1 vol by vol) and pipetted onto the poly-L-lysine treated sensor surface. The droplet was then dried and imaged at various illumination angles. Figure 7 shows the representative results of the experiment. The sample, which was not visible under top illumination, becomes distinguishable at higher incidence angles starting from 84° up to 90° due to changes in contrast between the shadow and the background intensity. The cells appear bright at higher incidence angles between 90° to 87° , while a faint shadow was visible at lower angles starting from 87° . These observations demonstrate the visualization of the bacterial samples with dimensions close to the pixel size of the sensor. In addition, the gray scale intensity-based quantification (Fig. 7(B)) shows a gradual decrease of the background brightness (y-axis, Fig. 7(B)) with an increase of the incidence angles from 90° to 84° (shades of green).

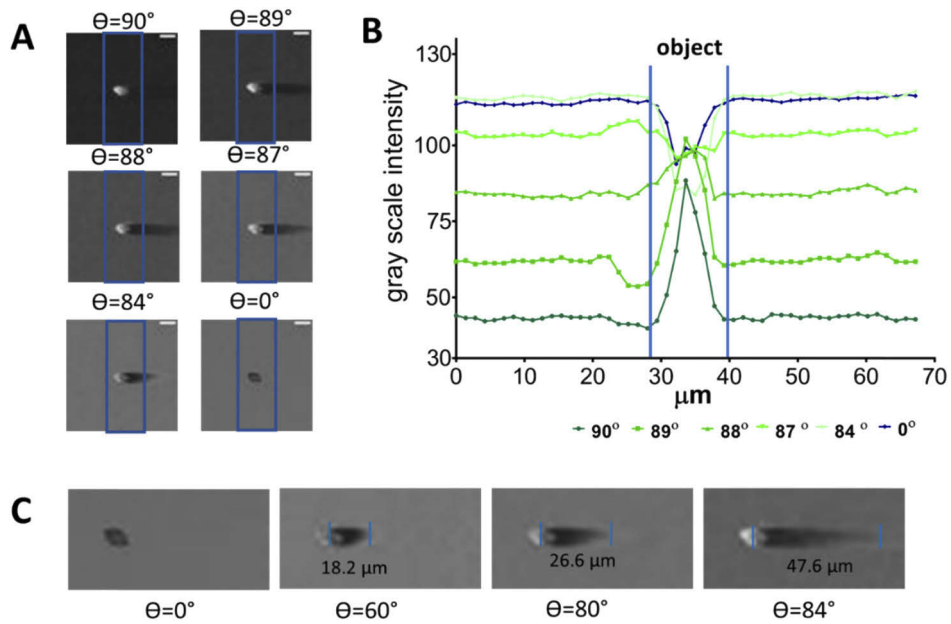


Fig. 6. Imaging *E. gracilis*. (A) *E. gracilis* at different illumination angles ranging from 0° to 90° . A gradual reduction in the background intensity is observed when the illumination angle is increased. (B) Graphical representation of the intensity profiles measured within the blue rectangle shown in panel (A). A 3-times drop of the background intensity with the increase of the incident angle reaching the maximum dark-field mode at 90° is observed. (C) Determination of the shadow length for the subsequent height calculation. (scale bars – 10 μm).

The scattering images show approximately 2-3 μm object width (across x-axis), that corresponds to the width of either a single bacterium or a doublet of bacteria (represented as short peaks) that is commonly known to form a doublet or clusters.

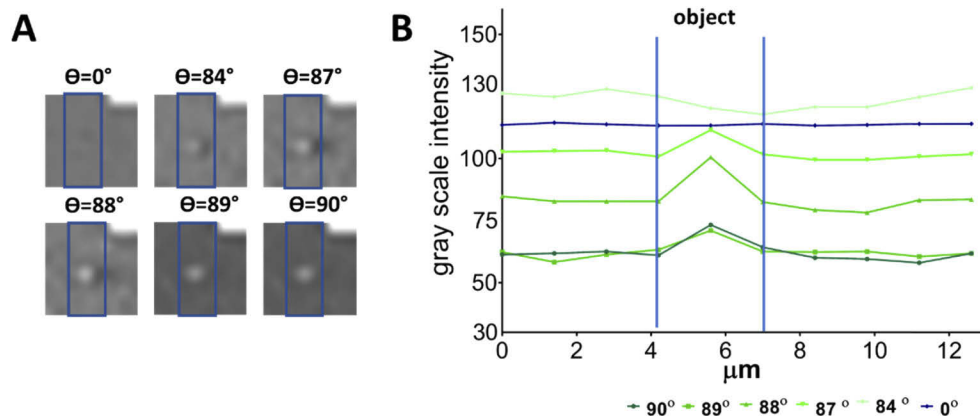


Fig. 7. Imaging of the fixed *S. epidermidis* under various angles of illumination. (A) The bacteria, which is of a size similar to the size of a pixel of the CMOS sensor, becomes visible under the large angles starting at 70° up to 90° angles. (B) Graphical representation of the data shows a two times drop in the background intensity at larger illumination angles due to Fresnel reflection and lower fill factor, which leads to better contrast (scale bar 5 μm).

In summary, the results demonstrate the ability of the presented platform to perform dark-field imaging of biological and non-biological objects over the full field-of view of an inexpensive CMOS sensor, as well as straightforward measurements of the height of micrometer-sized objects. The platform configuration allows us to perform experiments rapidly. However, the method has several limitations that could be improved by applying further engineering approaches. One such limitation is the increase of the sensor surface temperature during imaging, which restricts the use of this method for live biological samples. However, this issue could be potentially resolved by the addition of a heat sink that can reduce the temperature of the sensor. Another limitation of the system is that, at this point of development, it allows measurements of only fixed/dry samples.

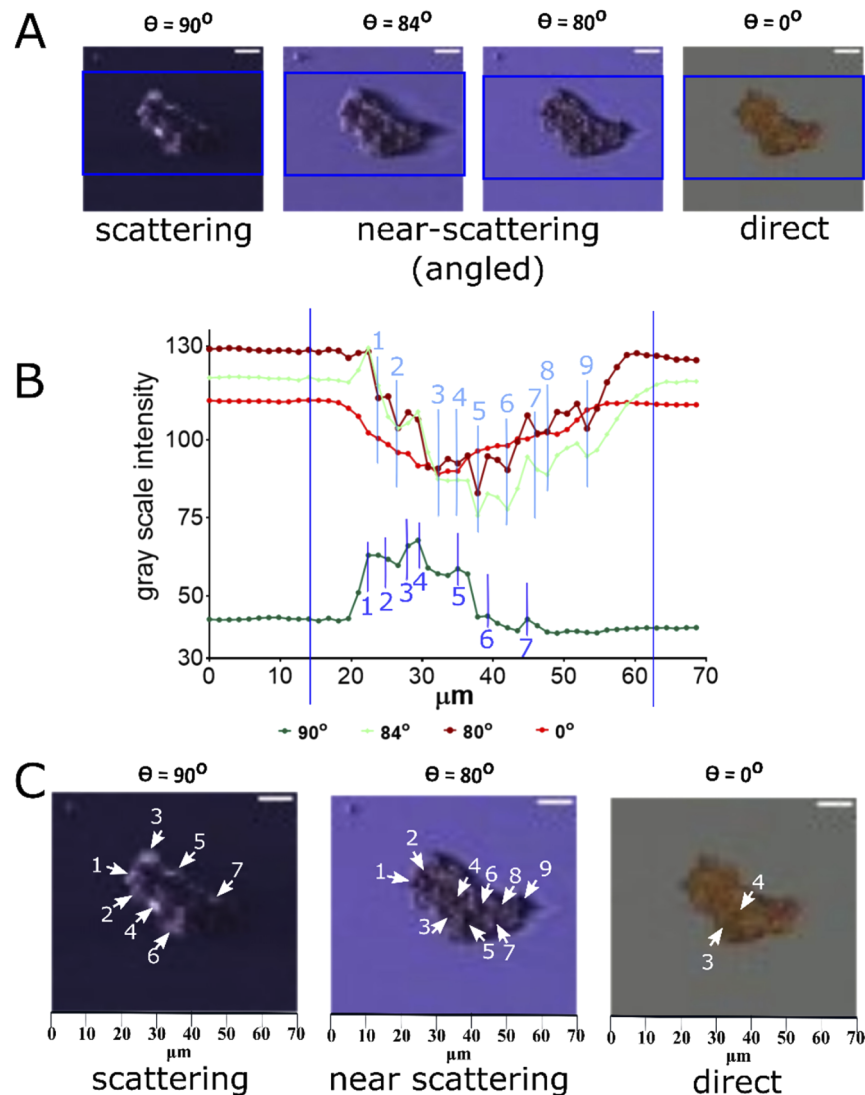


Fig. 8. Mapping pixel by pixel details of the biological samples at different angles. (A) *E. gracilis* cluster imaged under various angles of illumination. (B) Graph with pixel by pixel mapping based on the gray scale intensities calculated for the images, observed as peaks, labelled with numbers which are marked in the respective cluster of *E. gracilis* image at three different illumination angles (C).

In order to perform dark field imaging of liquid samples, further improvements to the system are necessary for refractive index matching.

3.3.2. Resolving features in a 3D cluster of single-celled algae (*E. gracilis*)

We imaged the cluster of *E. gracilis* using a multiangle illumination platform. Figure 8 represents the results of the pixel-by-pixel mapping of the *E. gracilis* cluster. The imaging and following analysis consider four different angles of illumination, such as scattering angle (90°), near scattering angles (84° and 80°) and top angle (0°). Figure 8(A) illustrates that, at scattering angles, the cluster of *E. gracilis* cells produces varying intensities of bright and dark spots, while in near scattering angles, the image appears as an overlap of bright field and dark-field images, with a unique observation of the dark pixels from dark-field imaging subsequently showing features of varying brightness intensity from near scattering illumination. The bright field illumination at top angle, showed no major variation of intensity although the cells appeared greenish, due to the chloroplast pigments. The gray scale intensities of the selective illumination angles, here 90° (Fig. 8(C) -left), 10° (Fig. 8(C) – middle) and 0° (Fig. 8(C) - right), shows a systematic pixel by pixel mapping of information that can be extracted from images using the presented set-up (shown as white arrows, labelled as numbers). This is performed by comparing the quantification graphs for three representative angles (Fig. 8(B)) to the corresponding images of the *E. gracilis* cluster (Fig. 8(C) – scattering, near-scattering and top images). The peaks marked as numbers in the graph could be mapped from the x-axis scale values of the graph to that of the x-axis scale of the image. Each number in the graph for a different illumination set-up maps to the corresponding gray scale intensity line in the graph with the same numbers marked for mapping either as pixel by pixel or as μm by μm across the x-axis of the graph and the image.

These mapping can be used for further elucidating the morphological differences within the cluster. Under the top illumination, the morphological characteristics of the cluster are not clear (only two discernible peaks). In contrast, changing the angle of incidence to 90° (7 discernible bright spots in image and peak in graph) and 84° to 80° (9 discernible bright and dark spots for both the graph and image) leads to the observation of distinguishable morphological features of the *E. gracilis* cluster (Fig. 8(B) and 8(C)). This analysis lead to the prediction of a total of 7-9 *E. gracilis* cells in the cluster. Such measurements show that this set-up can be used for analysis of microbial consortia without any post processing of the images. Furthermore, we were able to observe shadows cast by microspheres of different sizes as well as single protist/bacterial samples at near scattering angles, which combines both bright field and scattering characteristics within one image.

4. Conclusion

In this article, we demonstrated, for the first-time, dark-field microscopy directly on a CMOS sensor without the use of any lenses. This novel technique takes advantage of the fact that for incident light propagating from a medium with a lower refractive index (such as air) to a higher refractive index (such as plastic) at angles of illumination close to 90° , a larger fraction of light intensity is reflected, in accordance with the Fresnel equations of reflection. The larger the intensity of reflected light, the lower the background recorded by the CMOS sensor, leading to a reversal of the contrast of the object in dark-field mode vs. the bright field illumination mode, similar to that observed in lens-based dark-field microscopy modes. Individual objects and clusters of objects could be observed, for objects both larger and similar to the pixel size, highlighting the strength and robustness of the technique. In addition, using oblique illumination at angles between 0° and 85° we observed and quantified geometrical shadows of objects ranging in sizes from few micrometers to tens of micrometers. From simple geometrical considerations, we were able to calculate the height of these objects, in addition to their lateral dimensions that were determined from the bright field images.

The capabilities of the new imaging modality were tested on polystyrene beads of sizes ranging from 1.6 μm to 7 μm , where a three- to four-fold reduction of the background was observed for illumination at angles close to 90° vs. 0° . This is short of the expected > ten-fold background reduction (from Fresnel equations), largely due to the fact that the surface of the sensor is not flat. Improvements in the background reduction factor are expected if the surface flatness is increased by physical or chemical methods. For the 84° angle of illumination, shadow measurements of these polystyrene beads allowed for accurate height measurements, indicating the possibility of this technique to be used for 3D measurements of biological objects.

Next, we used these modalities for the imaging and quantification of biological samples that were fixed on the surface of the CMOS sensor. Single *E. gracilis* cells were imaged in both shadow and RDFM modes, which allowed for the calculation of height ($\sim 5 \mu\text{m}$) and length (10-11 μm). Fixed bacteria (*S. epidermidis*) were also imaged under various angles of illumination, demonstrating the ability of resolving and quantifying small, micrometer-sized biological objects. In addition, large clusters of *E. gracilis* algae were imaged to demonstrate the capability of the technique for quantifying 3D morphological features within colonies of microorganisms.

Overall, we demonstrated here a new platform for cost-effective, reflection-based dark-field microscopy modality (RDFM) directly on a CMOS sensor that allows for high spatial resolution (limited to the pixel size) and large field-of-view imaging of unstained, dried, or fixed biological and non-biological objects. In addition, this platform allows estimation of the height of micrometer-sized particles (via geometrical shadow measurements at oblique illumination) for the characterization of 3D morphological features. From a practical viewpoint, such measurements can be useful to understand different states of the cancerous cells, particularly during metastatic cancer cells studies, tissue generation, studying the effects of drug molecules on the cell membranes of cancerous cells [48] as well as effects on extracellular matrix materials [49]. The cancerous cells produce different levels of extracellular matrix, leading to variability in cellular thickness, cytoplasm to nucleus ratios and as a result to differences in morphology and cell mechanics [50]. These effects are challenging to be axially resolved for large FOV using a conventional microscopy technique without fluorescence or even with fluorescence requires confocal microscopy with extensive image post-processing and sample labeling [51]. In addition, quantitative phase imaging (QPI) has been applied to characterize morphological alterations of the cancer cells and has several advantages over conventional techniques, such as the ability to analyse live and unlabeled cells [52]. However, QPI method requires extensive image acquisition process with image-post processing and expensive equipment. Recently, 3D- on-chip imaging has been discussed widely for such applications [53], and the RDFM platform would fall in line with similar applications. Due to the low cost and simplicity, this technique can also be implemented for use in low resource environments for biological, medical, food safety, or environmental monitoring applications. Applications to the pathology field for the imaging of large, fixed (stained or unstained) thin tissue sections, and blood or cell culture smears are also possible, where the large field-of-view, coupled with the high spatial resolution and improved contrast, would provide an advantage over existing methods.

Funding

Natural Sciences and Engineering Research Council of Canada (Discovery Grant RGPIN-2018-05675, 238925, Discovery); Bolashak (Scholarship).

Acknowledgements

All authors made substantial intellectual contributions to the manuscript and approved it for publication.

This work was financially supported by the Natural Sciences and Engineering Research Council of Canada (NSERC), Discovery Grant RGPIN-2018-05675 (to S.W.-H.), Natural

Sciences and Engineering Research Council (NSERC) Discovery Project No 238925 (to D.V.N.); M.I. acknowledges the Bolashak International Scholarship for PhD studies.

Disclosures

The authors declare that the research was conducted in the absence of any commercial or financial relationships that could be construed as a potential conflict of interest.

References

1. J. Chalfoun, M. Majurski, T. Blattner, K. Bhadriraju, W. Keyrouz, P. Bajcsy, and M. Brady, "MIST: Accurate and Scalable Microscopy Image Stitching Tool with Stage Modeling and Error Minimization," *Sci. Rep.* **7**(1), 4988 (2017).
2. Z. J. Smith, K. Chu, A. R. Espenson, M. Rahimzadeh, A. Gryshuk, M. Molinaro, D. M. Dwyre, S. Lane, D. Matthews, and S. Wachsmann-Hogiu, "Cell-Phone-Based Platform for Biomedical Device Development and Education Applications," *PLoS One* **6**(3), e17150 (2011).
3. T. Gao, Z. J. Smith, T.-y. Lin, D. Carrade Holt, S. M. Lane, D. L. Matthews, D. M. Dwyre, J. Hood, and S. Wachsmann-Hogiu, "Smart and Fast Blood Counting of Trace Volumes of Body Fluids from Various Mammalian Species Using a Compact, Custom-Built Microscope Cytometer," *Anal. Chem.* **87**, 11854–11862 (2015).
4. C. W. Pirnstill and G. L. Coté, "Malaria Diagnosis Using a Mobile Phone Polarized Microscope," *Sci. Rep.* **5**(1), 13368 (2015).
5. Q. Wei, R. Nagi, K. Sadeghi, S. Feng, E. Yan, S. J. Ki, R. Caire, D. Tseng, and A. Ozcan, "Detection and Spatial Mapping of Mercury Contamination in Water Samples Using a Smart-Phone," *ACS Nano* **8**(2), 1121–1129 (2014).
6. T. S. Park, W. Li, K. E. McCracken, and J.-Y. Yoon, "Smartphone quantifies Salmonella from paper microfluidics," *Lab Chip* **13**(24), 4832–4840 (2013).
7. W. Bishara, T.-W. Su, A. F. Coskun, and A. Ozcan, "Lensfree on-chip microscopy over a wide field-of-view using pixel super-resolution," *Opt. Express* **18**(11), 11181–11191 (2010).
8. Y. Wu, Y. Luo, G. Chaudhari, Y. Rivenson, A. Calis, K. de Haan, and A. Ozcan, "Bright-field holography: cross-modality deep learning enables snapshot 3D imaging with bright-field contrast using a single hologram," *Light: Sci. Appl.* **8**(1), 25 (2019).
9. A. Ozcan and U. Demirci, "Ultra wide-field lens-free monitoring of cells on-chip," *Lab Chip* **8**(1), 98–106 (2008).
10. G. Stybayeva, O. Mudanyali, S. Seo, J. Silangcruz, M. Macal, E. Ramanculov, S. Dandekar, A. Erlinger, A. Ozcan, and A. Revzin, "Lensfree Holographic Imaging of Antibody Microarrays for High-Throughput Detection of Leukocyte Numbers and Function," *Anal. Chem.* **82**(9), 3736–3744 (2010).
11. Y. Zhang, H. Ceylan Koydemir, M. M. Shimogawa, S. Yalcin, A. Guziak, T. Liu, I. Oguz, Y. Huang, B. Bai, Y. Luo, Y. Luo, Z. Wei, H. Wang, V. Bianco, B. Zhang, R. Nadkarni, K. Hill, and A. Ozcan, "Motility-based label-free detection of parasites in bodily fluids using holographic speckle analysis and deep learning," *Light: Sci. Appl.* **7**(1), 108 (2018).
12. A. F. Coskun, T.-W. Su, and A. Ozcan, "Wide field-of-view lens-free fluorescent imaging on a chip," *Lab Chip* **10**(7), 824–827 (2010).
13. T.-W. Su, A. Erlinger, D. Tseng, and A. Ozcan, "Compact and Light-Weight Automated Semen Analysis Platform Using Lensfree on-Chip Microscopy," *Anal. Chem.* **82**(19), 8307–8312 (2010).
14. R. Delacroix, S. N. A. Morel, L. Hervé, T. Bordy, J.-M. Dinten, M. Drancourt, and C. Allier, "Cerebrospinal fluid lens-free microscopy: a new tool for the laboratory diagnosis of meningitis," *Sci. Rep.* **7**(1), 39893 (2017).
15. W. Xu, M. H. Jericho, I. A. Meinertzhagen, and H. J. Kreuzer, "Digital in-line holography for biological applications," *Proc. Natl. Acad. Sci.* **98**(20), 11301–11305 (2001).
16. O. Mudanyali, E. McLeod, W. Luo, A. Greenbaum, A. F. Coskun, Y. Hennequin, C. P. Allier, and A. Ozcan, "Wide-field optical detection of nanoparticles using on-chip microscopy and self-assembled nanolenses," *Nat. Photonics* **7**(3), 247–254 (2013).
17. F. Kazemzadeh and A. Wong, "Laser Light-field Fusion for Wide-field Lensfree On-chip Phase Contrast Microscopy of Nanoparticles," *Sci. Rep.* **6**(1), 38981 (2016).
18. T. Aidukas, R. Eckert, A. R. Harvey, L. Waller, and P. C. Konda, "Low-cost, sub-micron resolution, wide-field computational microscopy using opensource hardware," *Sci. Rep.* **9**(1), 7457 (2019).
19. G. Jin, I.-H. Yoo, S. P. Pack, J.-W. Yang, U.-H. Ha, S.-H. Paek, and S. Seo, "Lens-free shadow image based high-throughput continuous cell monitoring technique," *Biosens. Bioelectron.* **38**(1), 126–131 (2012).
20. A. Greenbaum, Y. Zhang, A. Feizi, P.-L. Chung, W. Luo, S. Kandukuri, and A. Ozcan, "Wide-field computational imaging of pathology slides using lens-free on-chip microscopy," *Sci. Transl. Med.* **6**(267), 267ra175 (2014).
21. M. Roy, D. Seo, C.-H. Oh, M.-H. Nam, Y. J. Kim, and S. Seo, "Low-cost telemedicine device performing cell and particle size measurement based on lens-free shadow imaging technology," *Biosens. Bioelectron.* **67**, 715–723 (2015).
22. A. Shanmugam and C. Salthouse, "Lensless fluorescence imaging with height calculation," *J. Biomed. Opt.* **19**(1), 016002 (2014).

23. F. Lang, M. Ritter, N. Gamper, S. Huber, S. Fillon, V. Tanneur, A. Lepple-Wienhues, I. Szabo, and E. Bulbins, "Cell Volume in the Regulation of Cell Proliferation and Apoptotic Cell Death," *Cell. Physiol. Biochem.* **10**(5-6), 417–428 (2000).
24. T. Key, A. McCarthy, D. A. Campbell, C. Six, S. Roy, and Z. V. Finkel, "Cell size trade-offs govern light exploitation strategies in marine phytoplankton," *Environ. Microbiol.* **12**(1), 95–104 (2010).
25. S. Taheri-Araghi, S. Bradde, J. T. Sauls, N. S. Hill, P. A. Levin, J. Paulsson, M. Vergassola, and S. Jun, "Cell-size control and homeostasis in bacteria," *Curr. Biol.* **25**(3), 385–391 (2015).
26. E. Henneman, G. Somjen, and D. O. Carpenter, "FUNCTIONAL SIGNIFICANCE OF CELL SIZE IN SPINAL MOTONEURONS," *J. Neurophysiol.* **28**(3), 560–580 (1965).
27. X. Fu, D. Huck, L. Makein, B. Armstrong, U. Willen, and T. Freeman, "Effect of particle shape and size on flow properties of lactose powders," *Particuology* **10**(2), 203–208 (2012).
28. R. Pal, "Effect of droplet size on the rheology of emulsions," *AIChE J.* **42**(11), 3181–3190 (1996).
29. U. Dusek, G. P. Frank, L. Hildebrandt, J. Curtius, J. Schneider, S. Walter, D. Chand, F. Drewnick, S. Hings, D. Jung, S. Borrmann, and M. O. Andreae, "Size Matters More Than Chemistry for Cloud-Nucleating Ability of Aerosol Particles," *Science* **312**(5778), 1375–1378 (2006).
30. Z. Göröcs and A. Ozcan, "On-chip biomedical imaging," *IEEE Rev. Biomed. Eng.* **6**, 29–46 (2013).
31. T.-W. Su, S. O. Isikman, W. Bishara, D. Tseng, A. Erlinger, and A. Ozcan, "Multi-angle lensless digital holography for depth resolved imaging on a chip," *Opt. Express* **18**(9), 9690–9711 (2010).
32. J. Kun, M. Smieja, B. Xiong, L. Soleymani, and Q. Fang, "The Use of Motion Analysis as Particle Biomarkers in Lensless Optofluidic Projection Imaging for Point of Care Urine Analysis," *Sci. Rep.* **9**(1), 17255 (2019).
33. X. Cui, L. M. Lee, X. Heng, W. Zhong, P. W. Sternberg, D. Psaltis, and C. Yang, "Lensless high-resolution on-chip optofluidic microscopes for *Caenorhabditis elegans* and cell imaging," *Proc. Natl. Acad. Sci.* **105**(31), 10670–10675 (2008).
34. T. Tanaka, T. Saeki, Y. Sunaga, and T. Matsunaga, "High-content analysis of single cells directly assembled on CMOS sensor based on color imaging," *Biosens. Bioelectron.* **26**(4), 1460–1465 (2010).
35. G. Zheng, S. A. Lee, Y. Antebi, M. B. Elowitz, and C. Yang, "The ePetri dish, an on-chip cell imaging platform based on subpixel perspective sweeping microscopy (SPSM)," *Proc. Natl. Acad. Sci.* **108**(41), 16889–16894 (2011).
36. A. C. Sobieranski, F. Inci, H. C. Tekin, M. Yuksekkaya, E. Comunello, D. Cobra, A. von Wangenheim, and U. Demirci, "Portable lensless wide-field microscopy imaging platform based on digital inline holography and multi-frame pixel super-resolution," *Light: Sci. Appl.* **4**(10), e346 (2015).
37. G. S. Verebes, M. Melchiorre, A. Garcia-Leis, C. Ferreri, C. Marzetti, and A. Torreggiani, "Hyperspectral enhanced dark field microscopy for imaging blood cells," *J. Biophotonics* **6**(11-12), 960–967 (2013).
38. R. M. Macnab, "Examination of bacterial flagellation by dark-field microscopy," *J Clin Microbiol* **4**, 258–265 (1976).
39. S. Enoki, R. Iino, N. Morone, K. Kaihatsu, S. Sakakihara, N. Kato, and H. Noji, "Label-Free Single-Particle Imaging of the Influenza Virus by Objective-Type Total Internal Reflection Dark-Field Microscopy," *PLoS One* **7**(11), e49208 (2012).
40. T. Wagner, H.-G. Lipinski, and M. Wiemann, "Dark field nanoparticle tracking analysis for size characterization of plasmonic and non-plasmonic particles," *J. Nanopart. Res.* **16**(5), 2419 (2014).
41. T. Wagner, A. Kroll, C. R. Haramagatti, H.-G. Lipinski, and M. Wiemann, "Classification and Segmentation of Nanoparticle Diffusion Trajectories in Cellular Micro Environments," *PLoS One* **12**, e0170165 (2017).
42. Z. Li, "Miniature optofluidic darkfield microscope for biosensing," in *Ultrafast Nonlinear Imaging and Spectroscopy II*, (International Society for Optics and Photonics, 2014), 91980G.
43. O. V. Grishin, I. V. Fedosov, and V. V. Tuchin, "Lens-free dark-field digital holographic microscopy for 3D tracking of microparticles," in *Saratov Fall Meeting 2014: Optical Technologies in Biophysics and Medicine XVI; Laser Physics and Photonics XVI; and Computational Biophysics*, (International Society for Optics and Photonics, 2015), 944816.
44. S. Kheireddine, A. Sudalaiyadum Perumal, Z. J. Smith, D. V. Nicolau, and S. Wachsmann-Hogiu, "Dual-phone illumination-imaging system for high resolution and large field of view multi-modal microscopy," *Lab Chip* **19**(5), 825–836 (2019).
45. S. Kheireddine, Z. J. Smith, D. V. Nicolau, and S. Wachsmann-Hogiu, "Simple adaptive mobile phone screen illumination for dual phone differential phase contrast (DPDPC) microscopy," *Biomed. Opt. Express* **10**(9), 4369–4380 (2019).
46. J. E. Corry, G. D. Curtis, and R. M. Baird, *Handbook of Culture Media for Food and Water Microbiology* (Royal Society of Chemistry, 2011).
47. R. Pal and A. K. Choudhury, *An Introduction to Phytoplanktons: Diversity and Ecology* (Springer, 2014).
48. R. Domura, R. Sasaki, Y. Ishikawa, and M. Okamoto, "Cellular Morphology-Mediated Proliferation and Drug Sensitivity of Breast Cancer Cells," *J. Funct. Biomater.* **8**(2), 18 (2017).
49. C. Walker, E. Mojares, and A. Del Río Hernández, "Role of Extracellular Matrix in Development and Cancer Progression," *Int. J. Mol. Sci.* **19**(10), 3028 (2018).
50. A. Pathak and S. Kumar, "Independent regulation of tumor cell migration by matrix stiffness and confinement," *Proc. Natl. Acad. Sci. U. S. A.* **109**(26), 10334–10339 (2012).
51. F. Pampaloni, E. G. Reynaud, and E. H. K. Stelzer, "The third dimension bridges the gap between cell culture and live tissue," *Nat. Rev. Mol. Cell Biol.* **8**(10), 839–845 (2007).

52. Y. Park, C. Depeursinge, and G. Popescu, "Quantitative phase imaging in biomedicine," *Nat. Photonics* **12**(10), 578–589 (2018).
53. Y. Zhang, Y. Shin, K. Sung, S. Yang, H. Chen, H. Wang, D. Teng, Y. Rivenson, R. P. Kulkarni, and A. Ozcan, "3D imaging of optically cleared tissue using a simplified CLARITY method and on-chip microscopy," *Sci. Adv.* **3**(8), e1700553 (2017).